THESIS

EXTREME RAINFALL MECHANISMS IN HURRICANE FIONA (2022)

Submitted by

Angelie Nieves Jiménez

Department of Atmospheric Science

In partial fulfillment of the requirements

For the Degree of Master of Science

Colorado State University

Fort Collins, Colorado

Spring 2025

Master's Committee:

Advisor: Michael M. Bell

Russ Schumacher
Brooke Anderson

ABSTRACT

EXTREME RAINFALL MECHANISMS IN HURRICANE FIONA (2022)

Hurricane Fiona's (2022) historical heavy precipitation devastated the Caribbean Island of Puerto Rico after it made landfall as a category 1 hurricane. Rainfall accumulation totals in southern interior region areas surpassed 900 mm during 18 – 19 September 2022. To analyze the rainfall mechanisms, we use output from the Hurricane Analysis and Forecast System (HAFS) configuration "B" modeling system and observations from the Puerto Rico Next Generation Weather Radar (NEXRAD) Level 2 Doppler radar and rain gauges around the island. Quantitative precipitation estimates from radar and rainfall measurements suggest that HAFSB simulated reasonably well the precipitation amounts and location. HAFSB track differences from the real trajectory contributed to discrepancies between the simulated and observed rainfall. We investigate three stages of the Hurricane Fiona rain event, each focusing on different processes. The first stage is associated with the primary eyewall and rainfall produced through boundary layer convergence. The second stage focuses on the principal rainband affecting the island and is associated with rainfall enhancement from vertical wind shear interactions with Fiona's potential vorticity. The third and final stage analyzes the enhancement of a "tail rainband" both over open water and the southern portion of the island as Hurricane Fiona kept strengthening west of Puerto Rico. Our findings support the hypothesis that evaporative cooling within inner core rainfall from stage one and two sets up a favorable environment for isentropic uplift to enhance rainfall production in stage three. Additional enhancements of the rainfall occurred over Puerto Rico's high terrain by orographic effects.

ACKNOWLEDGEMENTS

I dedicate this thesis to my grandmother, Teresita Blanes Palmer, who passed away just as I began my journey into the world of Atmospheric Sciences and Meteorology. She was a steadfast believer that I should pursue my dreams, trust my decisions, and that everything in life happens for a reason. Throughout this journey, my family has been my pillar: my mother, Angelie Jiménez Blanes; my father, Humberto Nieves Saldaña; my brother, Humberto Nieves Jiménez; my aunt, Maritere Jiménez Blanes; my uncle, José Matos; and my closest cousins, Fabiola Matos and Alexander Matos. I also want to acknowledge the loyal support of my emotional support animal, Nova, who has been by my side through it all. This journey began in 2022, when I took the significant step of moving from Puerto Rico to the continental United States. I knew I had made the right decision when I experienced the supportive, welcoming, and diverse community in the CSU Atmospheric Science Department and within my research group. Graduate school is about stepping outside your comfort zone, gaining experiences, and building connections, and I want to thank my advisor, Dr. Michael Bell, for his unwavering professional and personal support. His guidance, along with the encouragement and support of the Bell Group, has been invaluable to my growth in this field. I am also grateful for the friends I have made along the way, especially my closest friend, Katurah Zahler, and the Latin American community that has made me feel at home. My deepest thanks go to the professors who have equipped me with the foundations to become a well-rounded meteorologist, particularly my committee members, Dr. Russ Schumacher and Dr. Brooke Anderson, for their invaluable feedback and support. This work was supported by the National Science Foundation Graduate Research Fellowship No. (NSF 11-582).

TABLE OF CONTENTS

LIST OF FIGURES

INTRODUCTION

Tropical cyclones remain among the most destructive natural hazards worldwide. Additionally, the *National Oceanographic and Atmospheric Administration's (NOAA) National Centers for Environmental Information (NCEI) U.S. Billion-Dollar Weather and Climate Disasters (2023*) summary recognizes tropical cyclones among the costliest and deadliest weather disasters (NOAA NCEI, accessed 31/08/24). Scientists have extensively studied and recognized the structure, intensity, and impacts of tropical cyclones (TCs) with a significant focus on high wind impacts. The historical standard way of defining TC intensity is using the Saffir-Simpson Hurricane Wind Scale (SSHWS) which lacks consideration of heavy rainfall which is one of the most life-threatening risks to life and property (Saffir 1973, Simpson 1974, Rappaport 2014). Rainfall impacts to this day remain one of the most significant risks associated with TCs and will continue to do so in a warming and changing climate (Walsh et al. 2021, Klotzbach et al. 2022, Uehling and Schreck III 2024).

TC Structure & Rainbands

Early frameworks evaluating the ingredients leading to extreme rainfall and catastrophic flooding events are characterized by rainfall rate, event duration, or a combination of both (Doswell et al. 1996). The highest rain rates on average are found in the inner core of a TC which is mainly composed of the primary cyclonic circulation and associated strong convective precipitating primary eyewall and primary rainband (Barnes et al. 1983, Willoughby 1988, Houze 2010, Hence and Houze 2011). The outer core structure of a TC consists of secondary rainbands or "spiral bands", alternating from deep convection to shallow stratiform precipitation and whose rainfall intensity are uncorrelated with the inner core strength (Houze et al. 2006, Houze 2008, Hence and Houze 2012) but can produce locally heavy rainfall. Although TC rainfall can vary depending on spatial and temporal extent, dynamic and thermodynamic processes such as

moderate to strong vertical wind shear (VWS), diverse lifting mechanisms, environmental instability, and temperature gradients can alter its structure and intensity (Hence and Houze 2005; Schumacher and Johnson 2005; Yu et al. 2023). Past studies have focused on analyzing and understanding the factors and processes playing a role in heavy rainfall in mature TCs (Hence and Houze 2005). Findings support moderate-to-strong vertical wind shear (VWS) as one of the predominant factors affecting TC structure and rainfall distribution at a mature stage (Rogers et al. 2012, Reasor et al. 2013, DeHart et al. 2014). Rainfall displacement in TCs as a result of VWS and vortex tilt causes precipitation asymmetries and a strengthening downshear left quadrant of the TC (Black et al. 2002, Rogers et al. 2003, Boehm and Bell 2021, Liu et al. 2023). Subsequent studies examining principal rainband behavior in mature TCs using airborne radar data, attribute unique rainband squall line characteristics to storm behavior followed cold pool dynamics. Yu et al. 2015 and 2017 additionally suggest that additional factors such as cold pools and squall line effects can also play a role in outer rainband TC enhancement. Similar processes leading to supercell formation have also motivated studies focusing on outer rainbands, such as Morin and Parker 2011 and Wang et al. 2015. Several TCs in past years have presented an elongation and strengthening of their outer most rainband. This interesting feature has been observed by scientists in the field but has not been documented in its entirety. Nam (2021) evaluated a detached "monsoonal tail" rainband for Typhoon Jebi (2018) and found that VWS, moisture convergence, and low-level monsoon westerlies along with sub-seasonal variability enhanced convection in the southwestern quadrant of Typhoon Jebi. A similar behavior was seen in Typhoon Morakot (2009) due to low-frequency monsoon flows, the resulting influence on the slow movement of the storm and its asymmetric precipitation structure (Wu et al. 2011a, Wang et al. 2022). Unlike these typhoons, Hurricane Fiona did not reach a strong intensity with a well-defined eyewall structure but still managed to produce a "tail rainband" that contributed significantly to the total

accumulated precipitation of the event. Subsequently, while TCs share a general structure, their development is driven by distinct mechanisms for enhancement, influenced by storm dynamics and environmental conditions. As noted, the roles of strengthening TC rainbands in this elongated area of convection needs to be explored further and in other basins. Additionally, precipitation intensity remains a challenge in weak tropical cyclones due to the lack of a defined structure and its interaction with the environment (Nugent and Rios-Berrios 2017, Mazurek et al. 2023). As Hurricane Fiona left the island the Caribbean Island of Puerto Rico as a moderately sheared category 1 hurricane, the island experienced catastrophic rainfall amounts for two consecutive days. For this reason, I will be assessing Hurricane Fiona's rainfall contributions by defining stages and respective precipitation producing mechanisms including discussing the concept of what we call the "tail rainband".

Hurricane Fiona Synopsis

Hurricane Fiona (2022) was a damaging and long-lived TC that formed from a tropical wave that moved offshore from Africa on 7 September 2022. Disorganized and shallow convection were observed from satellite imagery as it moved westward across the tropical Atlantic. As the disturbance made its way toward the Lesser Antilles, it presented a more well-organized structure with a low-level circulation, and the National Hurricane center (NHC) named it Tropical Depression 7 (TD7) (NOAA NHC Hurricane Fiona Report 2023). TD7 kept strengthening and battling moderate to strong westerly VWS as it made its way toward the Caribbean and was upgraded to Tropical Storm (TS) Fiona on 1800 UTC 14 September (Figure 1a). Fiona maintained TS status until reaching the Caribbean Sea and intensifying into a Category 1 Hurricane at 1200 UTC on 18 September (NOAA NHC). Hurricane Fiona made landfall later that day over Puerto Rico as a Category 1 hurricane close to Punta Tocón, Lajas (National Weather Service -San Juan

(NWS-SJU) Hurricane Fiona report). After catastrophic flooding over the Puerto Rico and the Lesser Antilles, Hurricane Fiona continued to strengthen after making landfall in the Dominican Republic and turned into a major hurricane as it reached Turks and Caicos on 20 September. Fiona reached category 4 intensity as it moved northward into a more favorable environment and maintained the lowest pressure ever recorded to make landfall in Nova Scotia on 24 September. Hurricane Fiona (2022) was retired after this year due to its long-lived history and record-breaking impacts over Nova Scotia and the Caribbean.

Hurricane Fiona Records Over Puerto Rico

In the past 7 years, Puerto Rico has experienced three of the most damaging TC's in its history: Hurricane Irma (Sept. 2017; Category 5), Hurricane María (Sept. 2017; Category 4), and Hurricane Fiona (Sept. 2022; Category 1) (Castro and Lopez-Marrero 2020, Ramos-Scharrón et al. 2023). Noticeably, Hurricane Fiona stands out as the only non-major hurricane to severely affect the island in recent years. While not achieving a major hurricane status in the SSHWS near Puerto Rico, Hurricane Fiona devastated the island with historical amounts of rainfall. Ramos-Scharrón et al.'s 2023 hydrological analysis ranks Hurricane Fiona third in total maximum precipitation accumulation recorded in Puerto Rico since 1899. The authors attribute the unprecedented precipitation of this event to climate change indicators and saturated soils as contributing factors to the impacts. In this study I aim to further investigate the underlying dynamics and thermodynamics of Hurricane Fiona post-landfall.

Research Objectives and Hypotheses

This study focuses on analyzing the heavy precipitation associated with Hurricane Fiona over Puerto Rico and surrounding waters. Two of the primary mechanisms for rainfall generation are boundary layer pumping associated with the primary TC circulation and orographic lifting

over the complex terrain of Puerto Rico, which can combine to produce intense thunderstorms (Tu et al. 2024; Keellings and Hernández Ayala 2019). Satellite imagery, as shown in Figure 1, reveals an elongated area of deep convection that intensified before reaching the island. I hypothesize that the environment around and over the island was modulated by the passing storm, creating favorable conditions for rainfall enhancement. The observed enhancement over water away from the eyewall suggests the presence of additional rainfall mechanisms that warrant further investigation. The storm was affected by moderate vertical wind shear (5 m/s to 12 m/s) (VWS), which tilts the vortex and redistributes potential vorticity from the inner core to the outer regions, creating thermal and convective asymmetries (Deng et al. 2017, Boehm and Bell 2021). We hypothesize that this redistribution plays a crucial role in intensifying the rainfall event. Furthermore, we hypothesize that isentropic uplift associated with evaporative cooling from the prior rainfall enhanced the tail rainband after Fiona's passage.

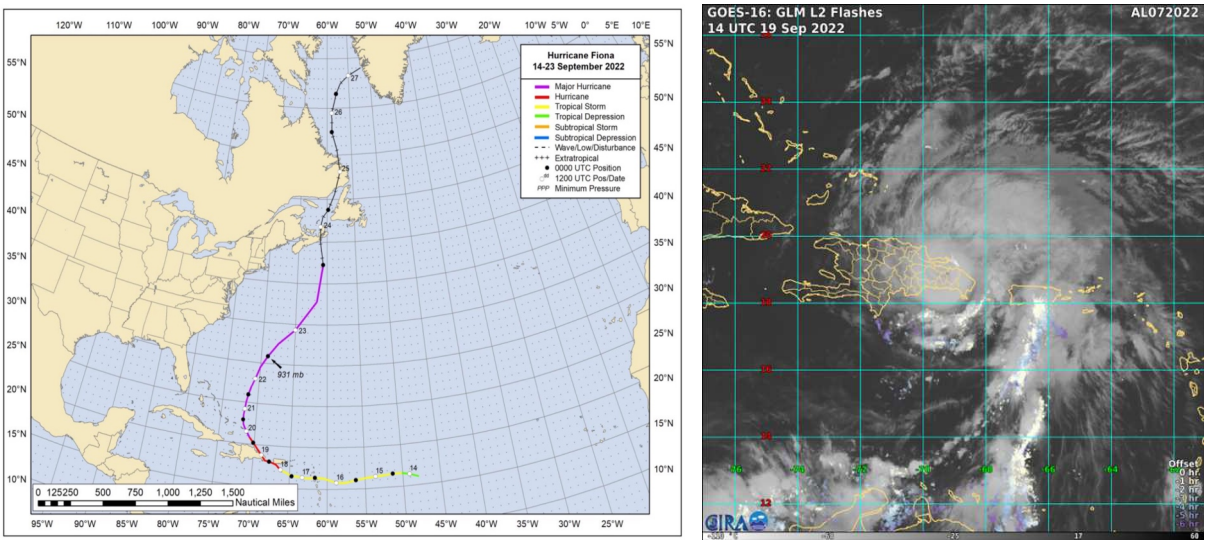

Figure 1. (a) Hurricane Fiona's track throughout its lifetime. Colors indicate storm strength. (b) Goes-16 visible (VIS) satellite image at 2022-09-19 at 1400 UTC showing the elongated tail-rainband.

Thesis Outline

Section 1 will describe the approach and available data to explore the topic. Section 2 will provide an overview of the precipitation estimates and measurements. Section 3 focuses on isentropic analysis and the lifting mechanisms for stages during and post-landfall. Section 4 presents the discussion and concise summary of the key points presented in this thesis.

METHODOLOGY AND APPROACH

Modeling

To evaluate the rainfall enhancing mechanisms in Hurricane Fiona during and post-landfall, we use the 2022 pre-operational Hurricane Analysis and Forecast System (HAFS) configuration "B" modeling system regional model from the Unified Forecast System (UFS) framework. HAFSB became newly operational for the 2023 hurricane season but was run in real time from 2019 through 2022 as part of the NOAA Hurricane Forecast Improvement Program (HFIP) (Alaka et al. 2022, Hazelton et al. 2024). HAFSB is based on the 2-way nesting capabilities of the finite-volume cubed sphere (FV3) dynamical core. The applied microphysics parameterizations include the Thompson cloud microphysics, the scale-aware Arakawa-Schubert (SAS) convection scheme, the Rapid Radiative Transfer Model for General Circulation models (RRTMG), the HYbrid Coordinate Ocean Model (HYCOM) coupling model, and a modified eddy-diffusivity mass-flux (EDMF) turbulent kinetic energy (TKE) planetary boundary layer (PBL) parameterization (Han and Bretherton 2019, Han et al. 2017, Thompson et al. 2004, Bleck 2002, Chen et al. 2022, Iacono et al. 2008). These parameterization schemes have been modified for hurricane environments based on recent research (Chen at al. 2023). The latitude and longitude size for the HAFSB parent domain is approximately 79^{o} x 79^{o}, with 6 km grid resolution, and 12^{o} x 12^{o}, with 2 km grid resolution for the storm following nest (Figure 2, Hazelton et al. 2023, Ramstrom et al., 2023; HAFSV0.3). For this analysis, we use the experimental 1-hr and 3-hr HAFSB model runs provided by NOAA's Atlantic Oceanographic and Meteorological Laboratory (AOML) Hurricane Research Division (HRD) to analyze the tail-rainband enhancing mechanisms from a dynamical standpoint.

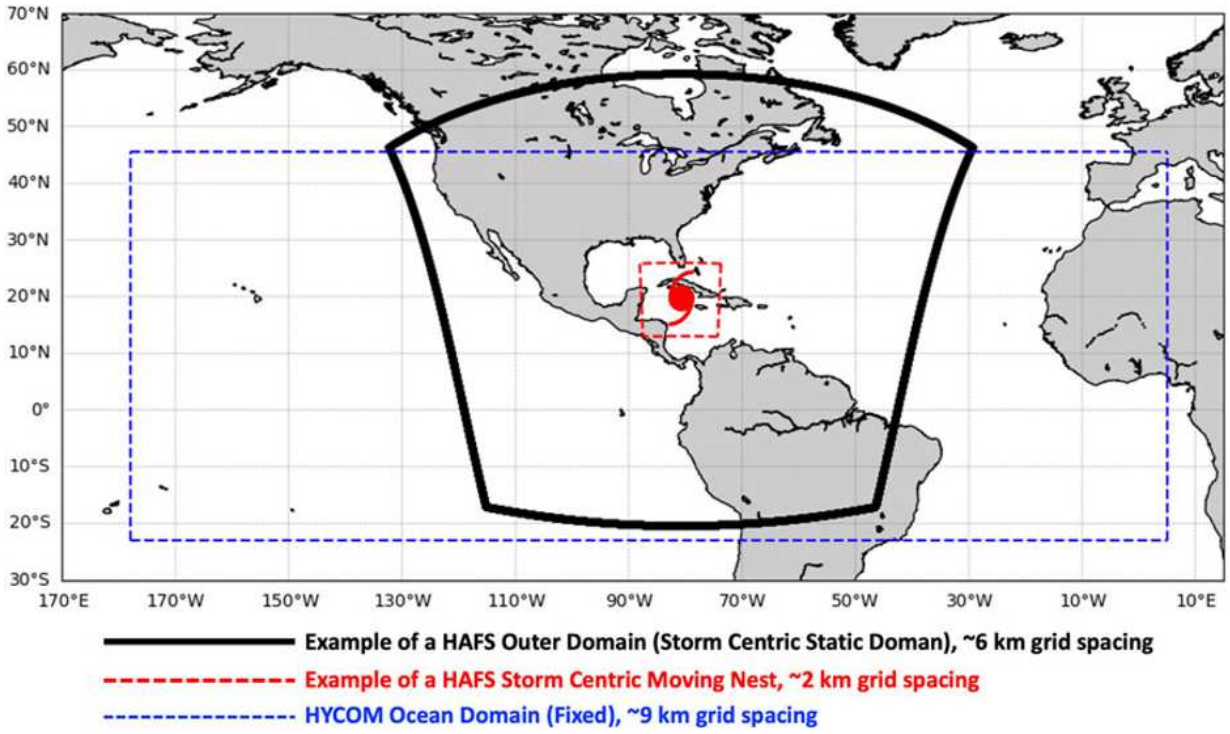

Figure 2. Example of the HAFSV0.3 grid configuration used in real-time in 2022. (Hazelton et al. 2023)

Observations

In this study, we also gather observations to gain an accurate understanding of the recorded precipitation over the island and estimate the accumulation over water. This observational data will be used in concert with our modeling results.

Next Generation Weather Radar Level 2 Ground Radar 1.1

The San Juan Next Generation Weather Radar Level 2 Doppler Radar (TJUA NEXRAD) is located approximately 901.6 meters above sea level on the Central Mountain Range (CMR) in Cayey, Puerto Rico, as seen in Figure 3. Due to the location of this S-band frequency radar, and the curvature of the earth, precipitation data is under sampled at low levels (Colom et al. 2010, Arias and Chandrasekar 2018, Acosta-Coll 2022). Data from this radar, collected approximately every 6 minutes, was acquired from the Amazon Web Services (AWS) open cloud server (NEXRAD on AWS accessed on January 25, 2024). The TJUA NEXRAD data was processed by

the Lidar Radar Open Software Environment (LROSE) co-developed by the National Center for Atmospheric Research Earth Observing Laboratory (NCAR/EOL) and Colorado State University (CSU) (DeHart et al. 2024). The LROSE tools used to calculate precipitation accumulation derived from the radar are the precipitation rate (RadxRate) and the accumulated quantitative precipitation (RadxQPE).

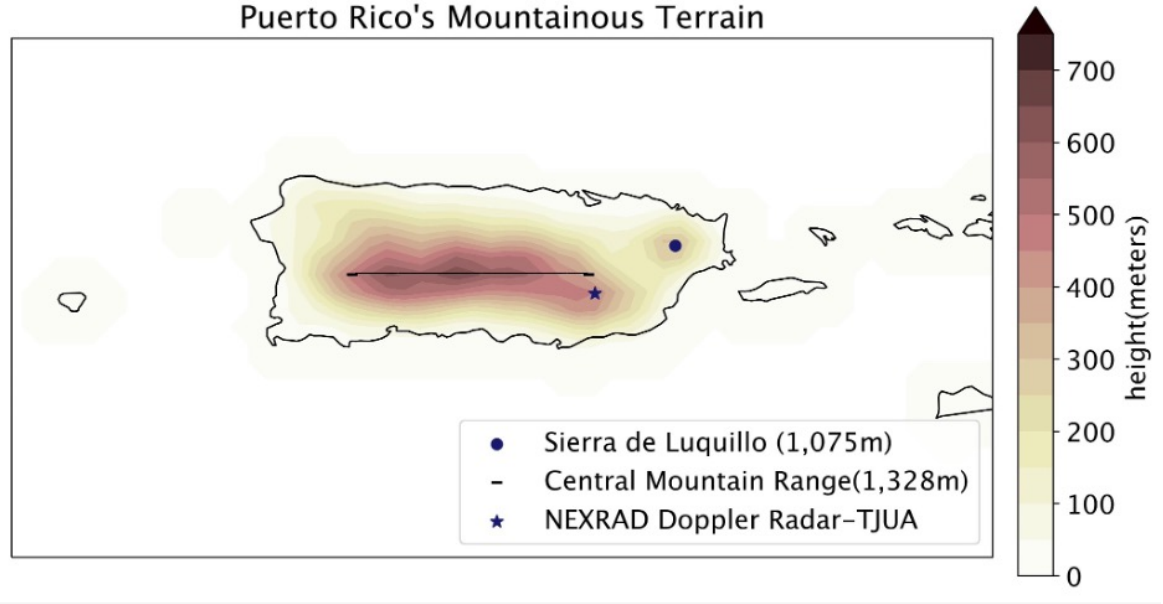

Figure 3. Topography map retrieved from HAFSB, representative of the simulation of the actual terrain Included are the height of the highest peaks of each mountainous regions and the location of the TJUA NEXRAD.

Rain Gauges 1.2

Rain gauge mesonets in Puerto Rico include stations from the United States Geological Survey (USGS), the National Oceanic and Atmospheric Administration (NOAA), the Cooperative Weather Observer Program (COOP), Community Collaborative Rain, Hail and Snow Network (CoCoRaHS), and United States Geological Survey (USGS) stations. Observed rainfall accumulation data over certain municipalities and sectors were processed and provided by the Puerto Rico Climatological Office and the National Weather Service in San Juan, Puerto Rico

(NWS-SJU). A total of 65 stations around the island provided daily precipitation data from 17 September to 19 September (Figure 4).

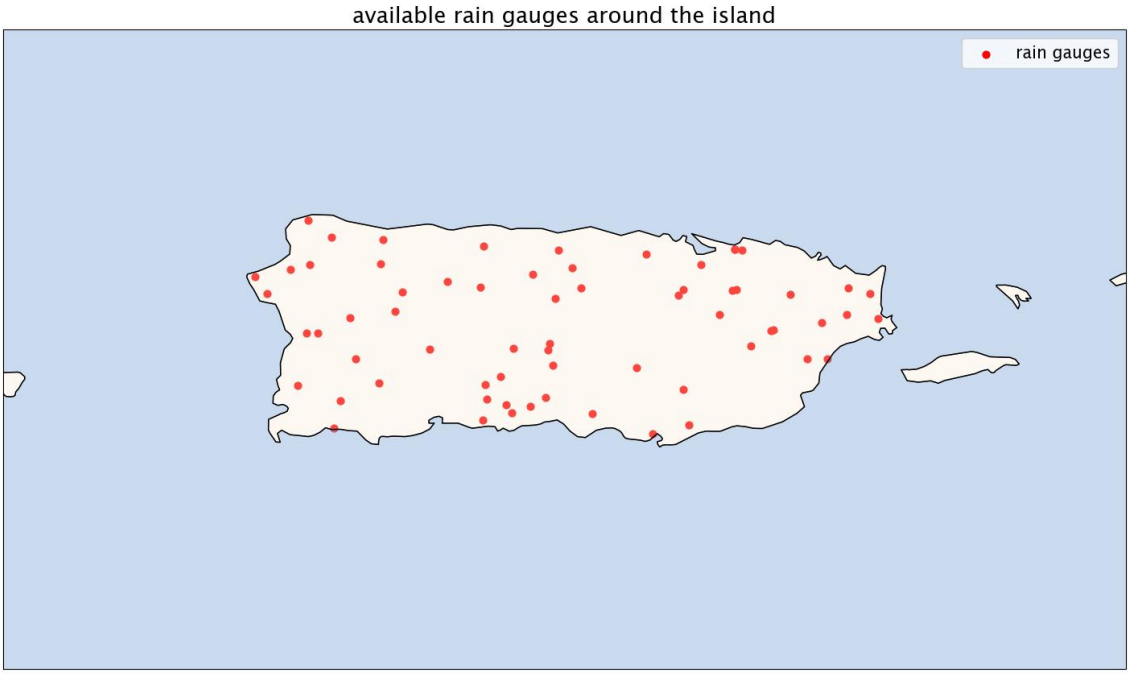

Figure 4 . Puerto Rico rain gauge network used in this study (n=65 stations).

RESULTS

Model Verification

The HAFSB model is primarily used in this study to aid in the reproducing and the understanding of some thermodynamic processes in Hurricane Fiona. We first compare the observations at hand, TJUA and rain gauges, with the HAFS simulation to determine the accuracy of the TC structure and rainfall locations and amounts produced by the model. For verification, we will focus on a 48-hour period that starts on 18 September 2022, at 0400 UTC and extends until 20 September 2022 at 0400 UTC (2022-09-18 12am LT – 2022-09-20 12am LT). A side-by-side concurrent comparison of the HAFSB model reflectivity of Fiona from the HAFSB with the GOES-16 infrared (IR) and visible (VIS) satellite image is shown in Figure 5. The comparison shows that HAFSB generally correctly represented the asymmetrical structure of Hurricane Fiona.

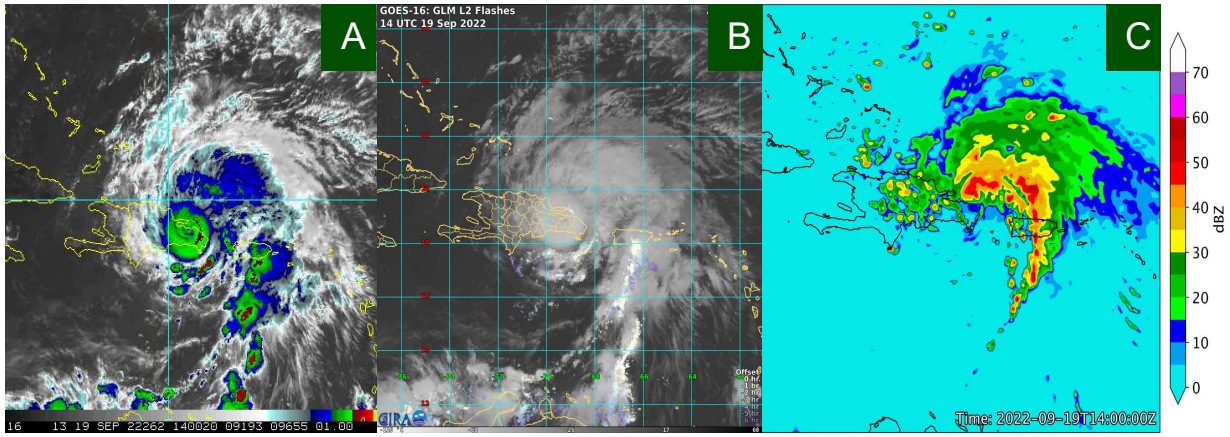

Figure 5. (a) GOES-16 Infrared (IR) (b) GOES-16 Visible Geostationary Lightning Mapper Level 2 (GLM L2) (c) HAFS-B radar reflectivity at 2022-09-19 at 1400 UTC.

While the panel present similar features, notable differences include the deep convection on the northern side of the island of Puerto Rico, which is absent in the satellite image. Another distinguishing difference is the location of the storm center which observations indicate made

landfall over Hispaniola while HAFSB tracks the storm just north of the island and slower. The GOES-16 IR (Figure 5a) image highlights the enhanced and detached nature of the principal rainband, with areas of strong convection south of Puerto Rico. HAFSB in Figure 5c captures an elongated feature of enhanced convection extending more than 450km from the primary rainband. HAFSB simulations managed to faithfully represent the rainband feature and hence, provide some justification for further analyzing the dynamics and thermodynamical characteristics of the rainband herein.

The resulting 48-hour rainfall accumulation comparison for the 18 – 19 September period is shown in Figure 6. The evaluation of the available data compares the observed rainfall accumulation of two types of measurements, the ground-based Doppler radar that retrieves precipitation estimates remotely and the rain gauges that record local measurements, with the HAFSB hourly rainfall rates over Puerto Rico and surrounding waters. Interpolated rain gauges along with TJUA's 48-hour derived rainfall accumulation serve as the event verification, however some accumulation differences between the two observations are observed. The TJUA data (Figure 6b) under samples some of the precipitation over the island especially over the CMR and south of the slopes. It is generally known that radar sampling plays a big role in surface precipitation retrieval estimates. TJUA's location is over the CMR and under sampling is common due to its high elevation, the radar range, and the enhancement of precipitation below the lowest radar beam from additional collision-coalescence. The HAFSB model successfully simulated the overall location and magnitude of the heavy rainfall associated with the island topography over the CMR and the Sierra de Luquillo regions for this event. However, the model overestimated rainfall over the northwestern region of the island as well as rainfall accumulation over northern waters in

Figure 6c. These significant values over the northern and eastern ocean regions and the northern areas of the island, are partly due to track differences from the actual storm.

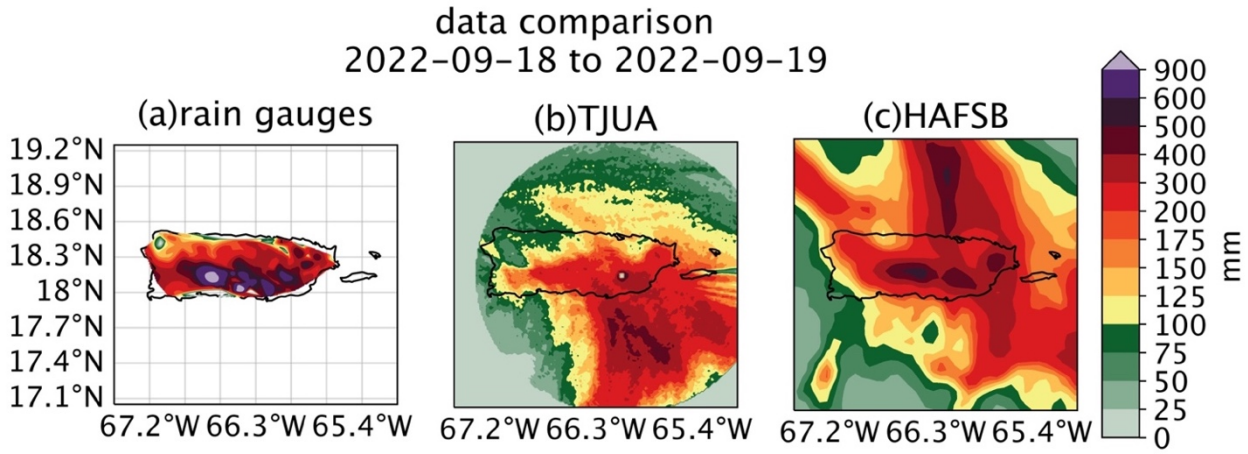

Figure 6. 48hr (2022-09-18 and 2022-09-19) precipitation accumulation comparison between the modeled and observed data (a) rain gauges, (b) TJUA radar, and (c) HAFS-B.

Figure 7 displays the NHC's best track for Hurricane Fiona along with the HAFSB simulated track. The NHC official track shows Hurricane Fiona making landfall in the southwestern corner of the island close to Punta Tocón, Lajas. The actual track produced the highest rainfall concentrations over the southern and mountainous regions of Puerto Rico. On the other hand, the HAFSB simulated Hurricane Fiona as making landfall along the southern region near Ponce, Puerto Rico, continuing across the island, and exiting along the northeastern coast. This shifted track to the northeast increases the precipitation over the Atlantic Ocean, eastern portion of the island, and over the southeastern ocean. On 19 September, the day after landfall, the HAFSB simulation situates the center of strengthening Hurricane Fiona north of the Dominican Republic, with an elongated rainband of deep convection and stratiform precipitation depositing more than 400 mm of rain over Puerto Rico's northern waters, over the island and south of the island. The differences between the observed precipitation and the HAFSB simulation can be attributed to differences in track and potential deficiencies in the model physics and initial

conditions. Despite these differences, the HAFSB accumulated precipitation generally aligns well with the observations and can be used for analysis of the physical mechanisms that produced heavy rainfall in the real world during the event.

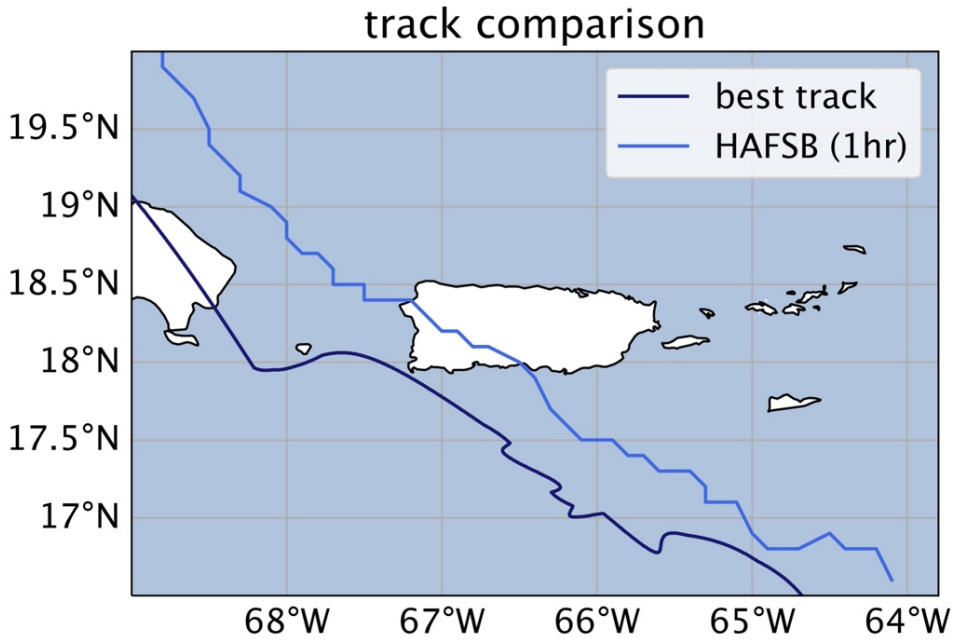

Figure 7. Hurricane Fiona's National Hurricane Center's (NHC) official storm track (dark blue) and the HAFSB hourly output storm track.

Rainfall Mechanisms

To better understand the environmental factors and detailed processes during Hurricane Fiona as it made landfall and traversed the island of Puerto Rico, we analyze the storm by dividing the event into 3 temporal stages. The first stage focuses on the rainfall associated with the primary eyewall while the storm's center was over the island. This time frame extends from 18 September 2022 from 0800 UTC to 19 September 2022, at 0000 UTC. The second stage focuses on the principal rainband affecting the island overnight from 19 September 2022, at 0000 UTC until 1200 UTC. The third and final time stage we analyze is the enhancement of the tail rainband over water and over the southern portion of the island as Hurricane Fiona kept strengthening over the Atlantic Ocean north of Hispaniola. The third stage starts on 19 September 2022, at 1200 UTC and extends until 20 September 2022, at 0000 UTC. This partitioning will be referenced throughout the rest of this study as Stage 1 (S1), Stage 2 (S2), and Stage 3 (S3), respectively.

Hurricane Fiona's asymmetrical precipitation structure is seen in Figure 8 for subplots a, b, and c. Stage S1 focuses on the rainfall associated with the inner core, while the center of the storm moved over the island. For this stage, the highest precipitation accumulation is coupled with the location of the storm's northeastern quadrant as well as the primary rainband. Hurricane Fiona's S1 (Figure 8d) is responsible for the highest rainfall amounts over waters on the eastern side as well as partially responsible for accumulations south of the CMR. Just prior to landfall on September 18th, there is available reconnaissance mission flight-level data as seen in Figure 9. This product from NOAA's Atlantic Oceanographic and Meteorological Laboratory (AOML's) Hurricane Research Division (HRD) aids to understand the observed storm's structure at specific levels merged from several 'swaths' into the storm. This flight-level tail Doppler radar (TDR) merged graphic at 1.5km presents the storm location and recorded areas of high dBZ. Reflectivity values

associated with precipitating stratiform, and convective regions surround the inner core and extend to the northeastern quadrant while stronger values are recorded in the primary rainband in the southeastern quadrant. The airborne Doppler radar may have underestimated the rainfall in the eyewall however, due to attenuation at X-band. Comparing the simulated HAFSB reflectivity structure in Figure 8a with the observed measurements in Figure 9, we can say that the HAFSB model was able to capture the convective strength of the primary rainband but overestimated the strength of the eyewall precipitation. The effect of shear on the storm dynamics and structure will be discussed further next.

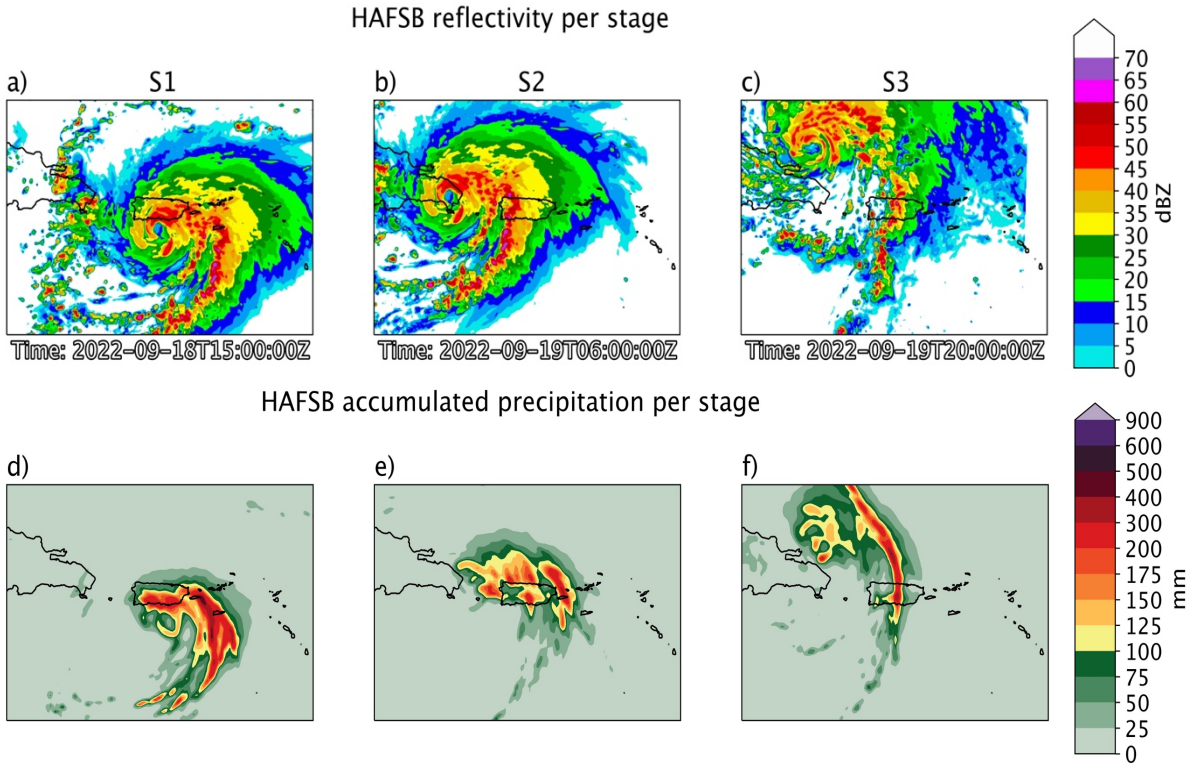

Figure 8. HAFSB reflectivity and accumulated precipitation panel comparison of (a) S1 (2022-09-28 1500 UTC), (b) S2 (2022-09-19 0600 UTC), and (c) S3 (2022-09-19 2000 UTC), respectively. (d) S1 precipitation accumulation time frame: 2022-09-18 0800 UTC – 2022-09-19 0000 UTC. (e) S2 precipitation accumulation timeframe: 2022-09-19 0000 UTC - 1200 UTC. (f) S3 precipitation accumulation time frame: 2022-09-19 12 -2022-09-20 0000 UTC.

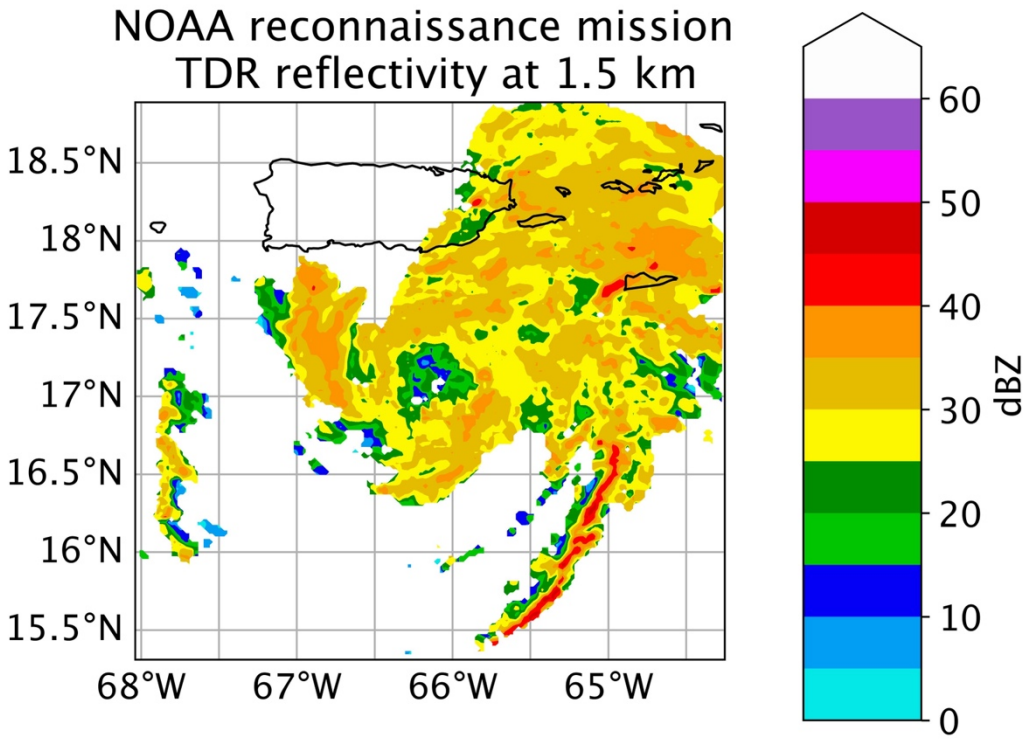

Figure 9. 1.5km flight-level Tail Doppler Radar (TDR) reflectivity mean composite from NOAA Hurricane Hunter's P-3 mission into Hurricane Fiona before landfall on 2022-09-18.

S2 shown in Figure 8b portrays the simulated reflectivity structure of the primary rainband over Puerto Rico while the center passed slightly north of the Dominican Republic. This stage is associated with heavy precipitation from the principal rainband and stratiform precipitation from the secondary rainbands. Figure 8e illustrates the location of the accumulated precipitation over the northern, eastern, and western waters around the island, with some accumulations over the central mountain range as expected by orographic lifting and convection modification over Puerto Rico as discussed in Hosannah et al. 2020. This stage accounts for most of the accumulation around the island and over the ocean. Recall, that earlier we mentioned that these total amounts were shifted slightly northeast due to track inconsistencies between the actual and the observed trajectory. It is also important to note that simulated inner core strength discrepancies may account for more precipitation than what was measured. During the last stage (S3), the center of the storm

was located at a considerable distance from Puerto Rico, as seen on Figure 8c, Nevertheless, this stage contributes the most significant rainfall to Hurricane Fiona's storm totals and catastrophic damage. Figure 8c also illustrates the structure of the detached section of the primary rainband, an area of high reflectivity south of the island that continued to strengthen as the storm moved farther away. Observations indicate that Hurricane Fiona's extended rainband was positioned further south than the tail rainband developed by HAFSB. However, I argue that the mechanisms HAFSB simulated to form what we define as the 'tail rainband' are likely consistent with the observed mechanisms.

Hurricane Fiona was affected by moderate to strong vertical wind shear (VWS > 5 m/s) throughout its lifetime. Our analysis averages the zonal (U) and meridional (V) wind components across the HAFSB storm nested domain at each vertical level. The resulting mean U and V wind components along the vertical profile for each stage are illustrated in Figure 10. The VWS, calculated between the 850 mb and 250 mb levels for each stage quantifies the shear magnitude the storm experienced according to HAFSB. These calculations indicate that the VWS slightly increased toward the end of Stage 3, increasing from 8.73 m/s to 10.9 m/s. A positive zonal wind component indicates westerly winds, while a positive meridional wind component indicates southerly winds. The results show that the VWS affecting Hurricane Fiona during our analysis was primarily southwesterly. The increase in wind speed with height (VWS) was stronger for the U component, reinforcing westerly shear effects on the asymmetrical precipitation structure observed.

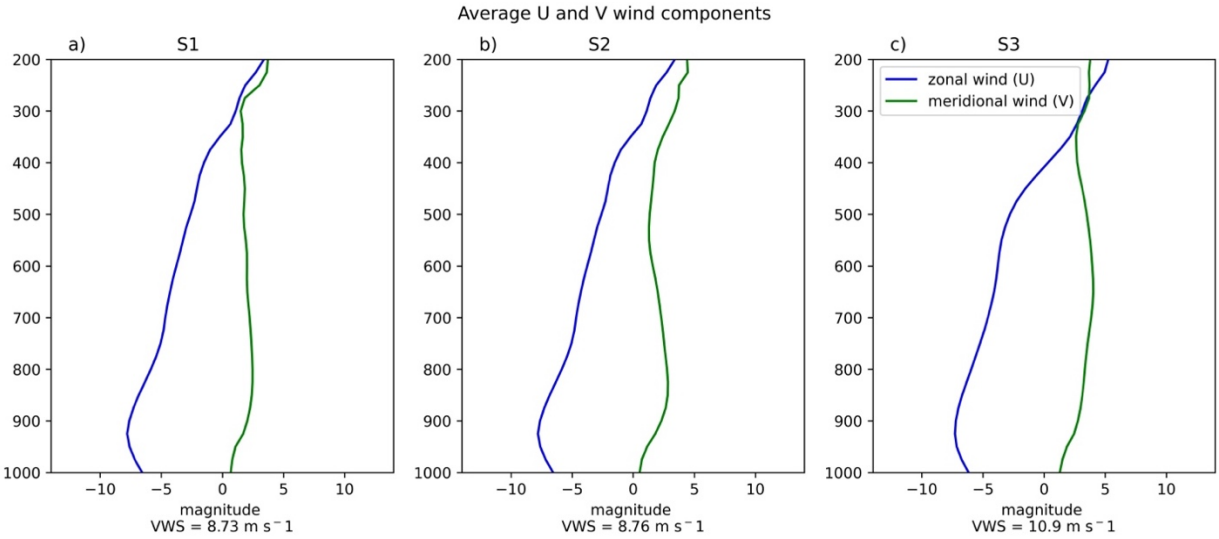

Figure 10. Mean vertical zonal and meridional wind components along the vertical profile. The VWS magnitude is also calculated for each stage using each U and V mean component.

Isentropic analysis enables researchers to estimate vertical motion in an adiabatic process, capturing the vertical and horizontal movement of air parcels along constant potential temperature surfaces in the absence of diabatic motion. In this analysis, I examine the dynamical and thermodynamical contributions at each stage using isentropic levels, where all fields are converted to isentropic coordinates and smoothed with a low-pass Gaussian filter to emphasize larger mesoscale motions and reduce small-scale noise. The use of isentropic levels in this study is due to the development of substantial meridional temperature gradients that affected the vertical motion, especially in stages S2 and S3. Figure 11 shows the positive (downward) and negative (upward) vertical motions for all stages at the 305K and the 325K isentropic levels, which correspond to approximately 1.5km and 8km, respectively. These levels were chosen to represent the low-levels and the mid-levels and diagnose vertical motions and heat exchanges. Vigorous updrafts shown in Figure 11a and 11d are associated with the eyewall, inner rainband, and primary rainband in S1. The strongest downdrafts appear ahead of the eyewall, while the most intense updrafts occur within the eyewall and the outermost rainband (ω=-4 Pa/s). The updraft strength in the primary

rainband extends and strengthens up to the 325K level (-4 Pa/s <ω < -12 Pa/s), surpassing the convective updraft strength observed in the eyewall. This coincides with the discussed structure of the storm evaluated with reconnaissance mission structure data where the primary rainband showed the strongest reflectivity values. On the other hand, vertical motions depicted in Figures 11b and 11e during S2 present a decrease in the strength of rising motions in the primary rainband due to the storm's interaction with the island but are still present south of the island. For this stage, it is important to note that areas of strong updrafts are coupled with areas of highest precipitation described in Figure 8e. Vertical motion activity increases south of the island in S3 where there is a broad area of increased negative values south of Puerto Rico. This is the area where the enhanced tail rainband is located (Figure 8c). At the 325K isentropic level, these updrafts are further amplified, exceeding -4 Pa/s (Figure 11f).

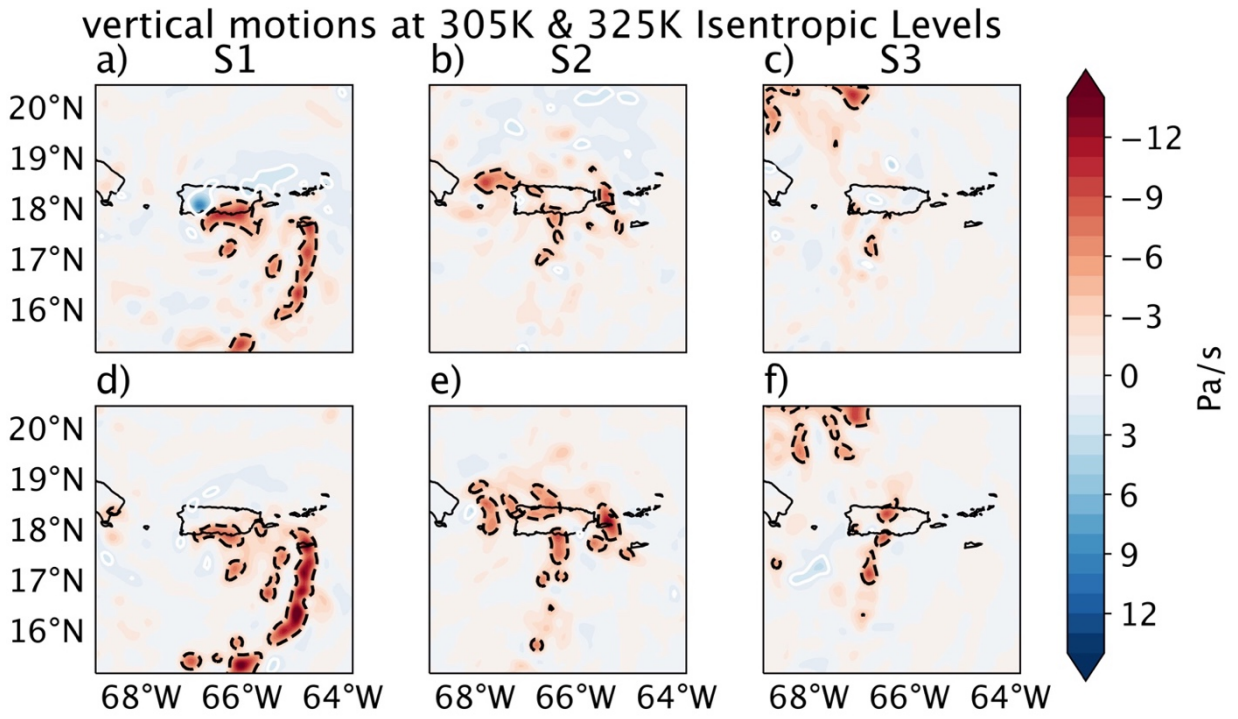

Figure 11. All vertical motions (shaded contours) with emphasis in strongest vertical motions (closed black/white contours) for each stage at an instantaneous time at a 305K isentropic level (a,b,c) and 325K isentropic level (d,e,f). Closed white contours indicate downward motions (ω=2 Pa/s). Closed black contours indicate strong rising motions (ω=-4 Pa/s). (a,d) S1 2022-09-18 at 1500 UTC (b,e) S2 2022-09-19 at 0600 UTC (c,f) S3 2022-09-19 at 2000 UTC.

TCs in the Northern Hemisphere are associated with positive potential vorticity (PV) and are generally considered large-scale PV systems. On isentropic surfaces, PV can be interpreted similarly to absolute vorticity (AV), since it is defined as the dot product of AV and static stability of the fluid on an isentropic surface. In Figure 12, we examine the AV on an isentropic surface to assess the dynamic and thermodynamic factors contributing to the enhancement of the tail rainband. The vorticity associated with S1 at the 305K low level is notably concentrated within the storm's inner core, where strong convective updrafts (dashed contours) are expected (Figure 12a). The upshear right quadrant, followed by the downshear right quadrant, shows enhanced

absolute vorticity and vertical motions, while the downshear left and upshear left quadrants lack significant vorticity enhancement. Most of the strong updrafts are coupled with potential vorticity in the downshear right quadrant of the system, ahead of the system there is an absence of AV, which is expected. For S2, the absolute vorticity reflects the sheared and dispersed placement of the secondary rainband (Figure 12b). During S3, strong updrafts and downdrafts are observed over the ocean, where tail-rainband enhancement occurs before landfall. This indicates an active thermodynamic process, which will be explored further in this study. This panel illustrates the evolution of AV associated with Hurricane Fiona, beginning as a compact, concentrated area of positive AV that gradually expands due to the effects of land interaction and vertical wind shear.

In a sheared environment, the structure of a tropical cyclone can be significantly impacted, and in the case of Hurricane Fiona, vertical wind shear altered the distribution and location of AV. Figure 12d, 12e, and 12f present AV at the 305 K (colored contours) and 325 K (closed contours) isentropic levels, allowing us to examine the storm's vertical structure and the influence of shear on its upper levels. The tilting evident in the AV structure, particularly at the 325 K isentropic level, suggests that the upper portions of the system are displaced relative to the lower levels. The location of the high AV is associated with the storm's decent motions in the center. This tilt is more pronounced in the outer areas of the rainband, where the sheared AV component at 325 K highlights the asymmetry imposed by the environmental shear. Such structural changes in AV under shear conditions can influence the cyclone's intensity and organization, impacting rainfall distribution and storm evolution as the AV core shifts or elongates in response to varying atmospheric forces.

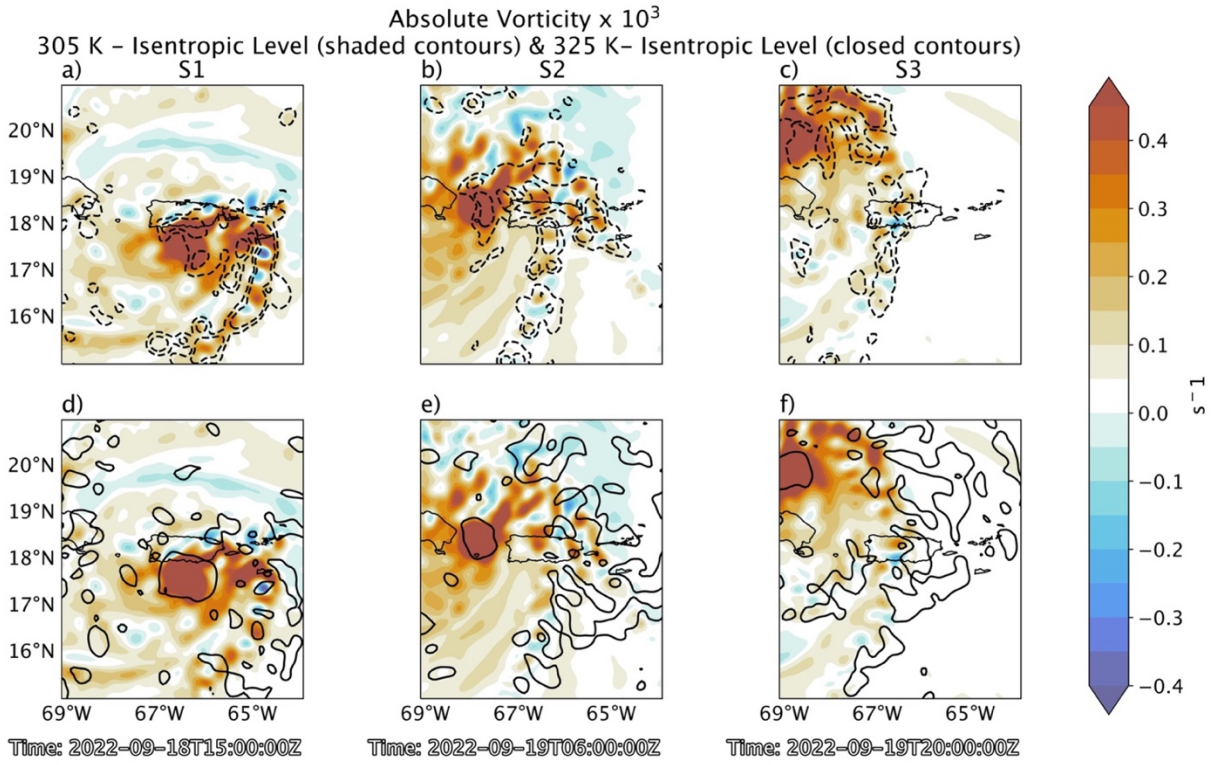

Figure 12.Absolute vorticity (shaded contours) at the 305K isentropic level with vertical motions (dashed contours) and absolute vorticity at the 325K isentropic level (closed contours) for each stage at an instantaneous time. Dashed contours indicate magnitudes between -4 Pa s^{-1} and -1Pa s^{-1}. Closed contours indicate magnitudes between 0 s^{-1} and 0.5 s^{-1}. (a) S1 2022-09-18 at 1500 UTC (b) S2 2022-09-19 at 0600 UTC (c) S3 2022-09-19 at 2000 UTC.

Tropical environments usually present barotropic characteristics because of the lack of substantial density or temperature gradients. We hypothesized that with the passing of Hurricane Fiona and its rainbands over the area of Puerto Rico, the environment is modulated and baroclinic characteristics develop. Observing this aspect from a 305K isentropic level standpoint provides the point of view needed to evaluate the behavior air parcels ability the level of free convection (LFC) more effectively after this environmental modulation.

On an isentropic surface, such as the 305 K level shown in Figure 13, air parcels move from high to low pressures along the same isentrope in adiabatic flow. Isentropic lifting refers to

the movement of an air parcel along an upward-sloping isentropic surface. For initial S1 and S2 (Figure 13a and 13b), the low-pressure system is being embedded in a baroclinity background connected to the shear discussed earlier, and the storm's trajectory modifies the north-to-south pressure gradient. While this storm moves over the island, the isentropic pressure behind is altered creating a significant gradient and increasing instability much like presenting baroclinic characteristics. S1 and S2 set up environmental modifications that drive air parcels in S3 to rise on its south-to-north path (indicated by the light green to blue shades), cooling and condensing to form stratiform clouds and precipitation within the rainbands. Figure 13c shows the pressure gradient aligned with the storm's path, with a predominately north-south component. As Hurricane Fiona passed over Puerto Rico, three primary lifting mechanisms were at play: isentropic lifting south and north of the island, orographic lifting over the island, and buoyant lifting from convective instability.

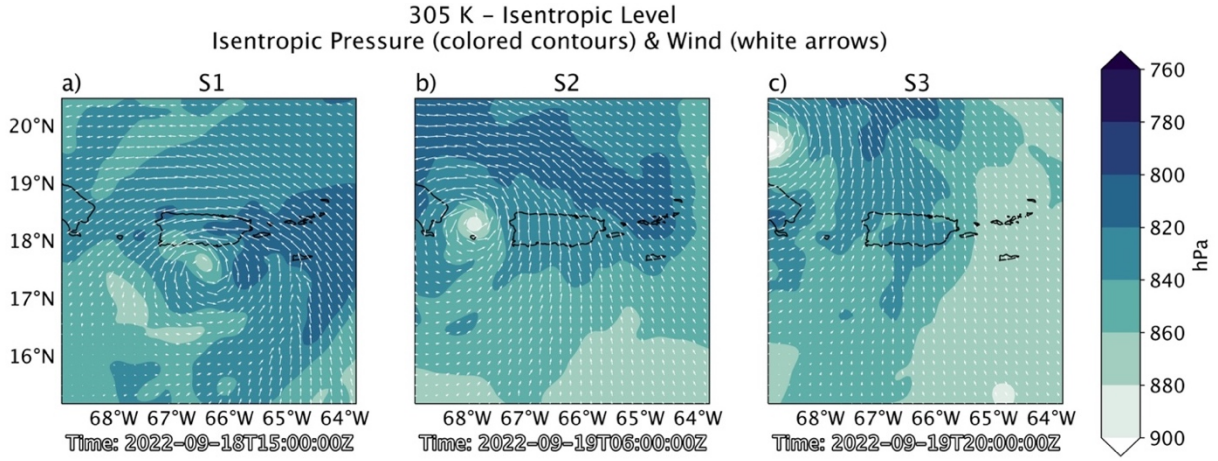

Figure 13. Atmospheric pressure (colored contours) and winds (white arrows) for all stages at the 305K isentropic level at instantaneous times (a) S1 2022-09-18 at 1500 UTC (b) S2 2022-09-19 at 0600 UTC (c) S3 2022-09-19 at 2000 UTC.

The omega (ω) equation for vertical motion in isentropic coordinates can be written as:

$$\omega = \frac{Dp}{Dt} = \frac{\delta P}{\delta t} + u\,\frac{\delta p}{\delta x} + \boldsymbol{v}\,\frac{\boldsymbol{\delta P}}{\boldsymbol{\delta y}} + \dot{\theta}\,\frac{dp}{d\theta}$$

where omega is the material change in pressure (p) on the isentrope. The partial derivative with respect to time indicates the motion of the isentrope itself, and the two horizontal advection terms are the vertical motion associated with adiabatic flow along a sloping isentropic. The isentropic lift is analogous to vertical motion over a mountain, where pressure takes the place of terrain height. The final term is due to diabatic heating ($\dot{\theta}$) in a stably stratified atmosphere. Figure 14 shows the individual contributions to omega on the 305 K surface during stage 3. In Figure 14a negative values correspond to regions where the meridional wind interacts with the pressure field, leading to a coupling between isentropic uplift and vertical motions. Upward motion is found over much of the domain where the southerly flow associated with the cyclonic rotation of the TC encounters the sloping isentrope to the north. Over Puerto Rico, descending motion occurs on the leeward side of the mountains. The meridional component of isentropic lift at 305 K is generally much

stronger than the zonal component shown in Fig. 14b, but the zonal component also contributes to positive lifting in many locations.

The cross-isentropic flow provides a quantification of the vertical motion associated with convective heating and cooling. Since potential temperature (θ) increases with height while pressure decreases in a stably stratified atmosphere, $\frac{dP}{d\theta}$ is negative at all levels. Condensational heating results in a positive $\dot{\theta}$ and evaporative cooling results in a negative $\dot{\theta}$, such that omega has the opposite sign of the heating where negative omega (ω) signifies upward motion. At the 305 K level (Fig. 14c) the heating term is positive throughout much of the domain indicating downward motion and the predominance of low-level evaporative cooling. The cooling is associated with the widespread rain from the rainband complex. There is upward motion over Puerto from this term, indicating condensational heating associated with orographic uplift on the windward side of the mountain. The meridional pressure advection and diabatic heating terms largely cancel throughout much of the domain except in the rainband region, resulting in low-level upward motion near Puerto Rico and to the north. At the 325 K isentropic level in Fig. 15, the zonal pressure advection term is more dominant due to more westerly winds. Given the higher level in the atmosphere, the diabatic heating term (Fig. 15c) it is likely associated with condensational heating and freezing in deeper convection (Figure 15c). Since the 325 K level is near the zero-degree isotherm there may also be some cooling related to melting.

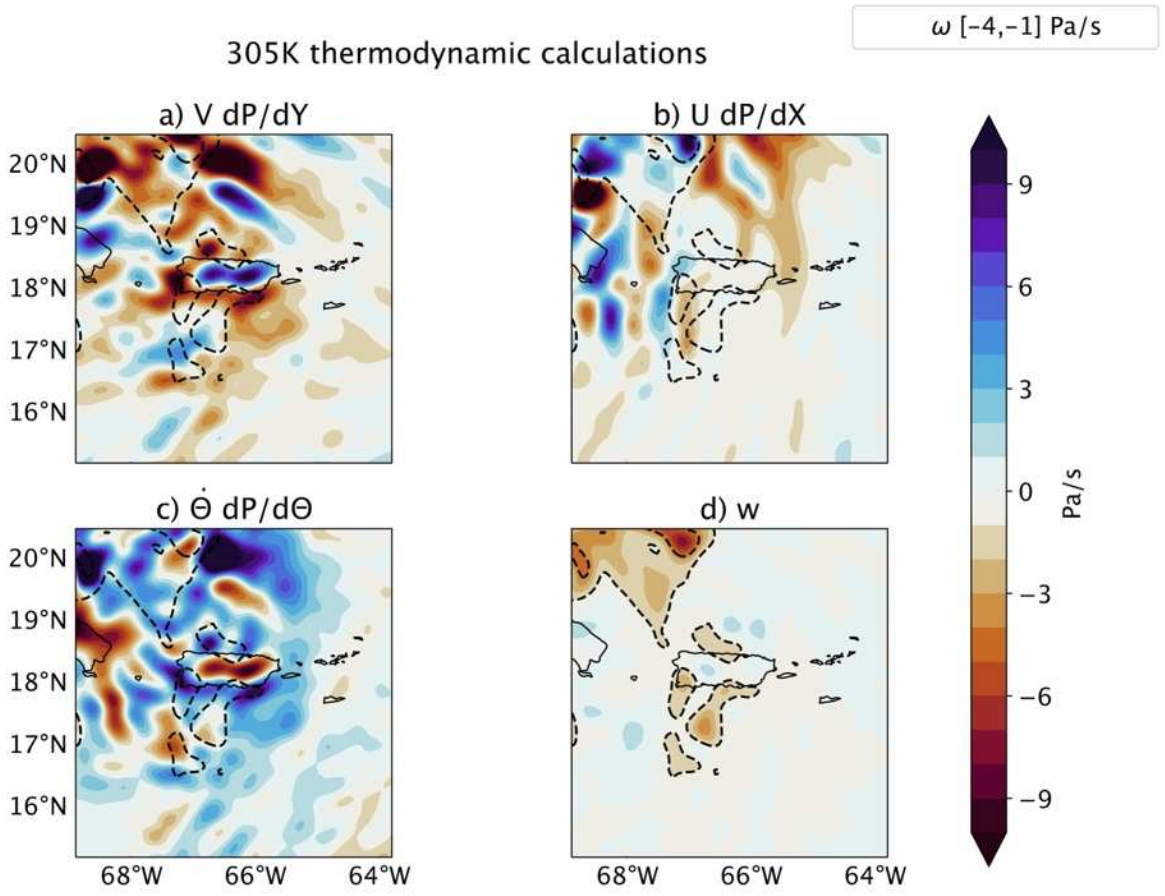

Figure 14.(a)V dP/dY (colored contours), (b) U dP/dX (colored contours), (c) $\dot{\theta}\ \frac{dP}{d\theta}$ *(colored contours), (d)* ω *(colored contours), and vertical motions (closed dashed contours) for Stage 3 at the 305K isentropic level at an instantaneous time 2022-09-19 at 2000 UTC. Vertical motions indicate a magnitude of -4Pa/s.*

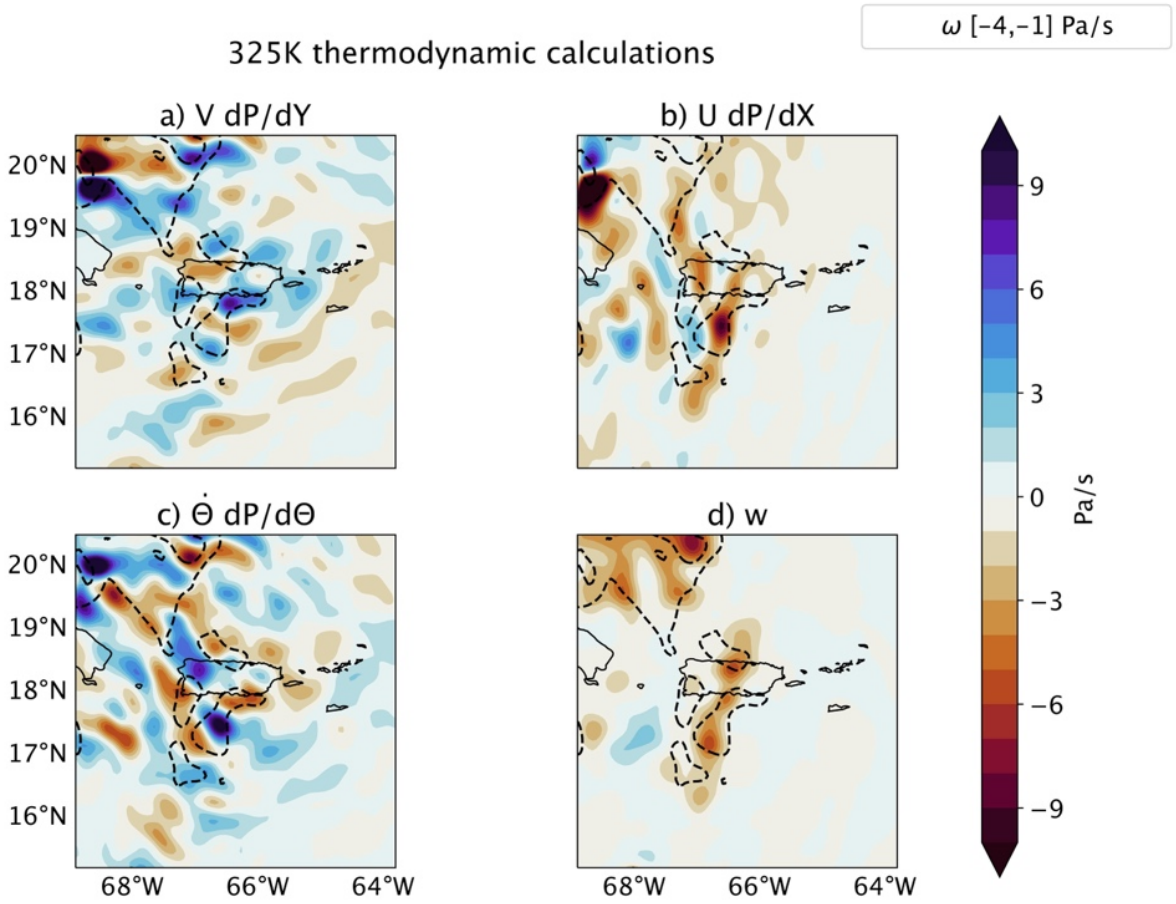

Figure 15. (a)V dP/dY (colored contours), (b) U dP/dX (colored contours), (c) $\dot{\theta}\ \frac{dP}{d\theta}$ *(colored contours), (d)* ω *(colored contours), and vertical motions (closed dashed contours) for Stage 3 at the 325K isentropic levels at an instantaneous time 2022-09-19 at 2000 UTC. Vertical motions indicate a magnitude of -4Pa/s.*

OTHER INFLUENCING FACTORS

Frontogenesis 2.1

Past studies have shown the presence of a frontogenesis in aiding TC intensification while other studies have suggested the presence of frontogenesis in TC rainbands (Shin and Zhang 2017; Powell and Bell 2019; Ruan et al. 2023). In the context of a TC, frontogenesis can indicate regions where strong temperature gradients and convergence are enhancing the storm's structure. Figure 16 shows the calculation of the 950 mb frontogenesis around Hurricane Fiona for our three different stages, highlighting changes in the storm's temperature gradients. Results indicate that there is weak frontogenesis occurring. Initially in S1, frontogenesis values of around 1.0 K m-1 s-1 are concentrated near the cyclone's inner core and primary rainband. This setup likely contributes to the asymmetric distribution of precipitation downshear and upshear right of the storm of the strengthened primary rainband.

As the storm evolves, S2 and S3 frontogenesis areas in Figure 16b and 16c become more elongated and shift toward the west and southwest, indicating the continuous development of an asymmetrical structure influenced by factors like land interaction and VWS. In the later stage, strong frontogenesis extends farther from the center, showing that rainbands are now located at a greater distance. This shift increases the likelihood of heavy, localized rainfall in the outer regions, aiding in the development of the tail-rainband and raising the risk of flooding in Puerto Rico. Although frontogenesis is not the primary lifting mechanism in this tail-rainband, it contributes slightly to its formation and strength.

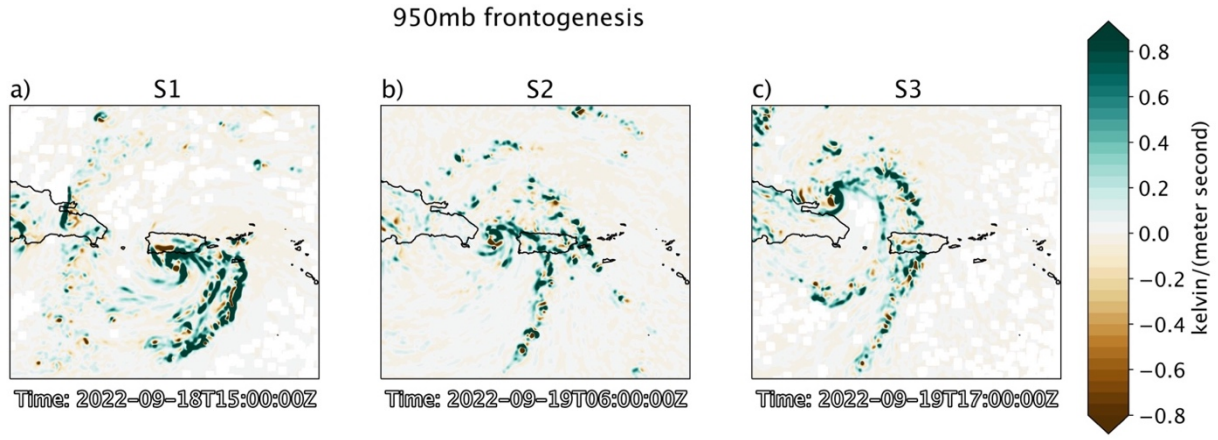

Figure 16.Frontogenesis at 950mb for all stages, respectively. a) S1 2022-09-18 at 1500 UTC (b) S2 2022-09-19 at 0600 UTC (c) S3 2022-09-19 at 2000 UTC.

Low-level inflow 2.2

Figure 17 illustrates the 1000 mb low-level inflow around Hurricane Fiona, with wind vectors and geopotential height (gpm) contours. The inflow pattern in the rainband region shows a concentration of organized low-level winds directed toward the cyclone's center. The geopotential height gradients indicate a pressure decrease toward the center, which drives the low-level convergence through a force imbalance in the boundary layer. The strongest inflow aligns with the lighter shaded areas, where the wind vectors suggest a pronounced inflow from the south, southwest, and southeast. This configuration enhances the rainband's development by promoting upward motion, which supports convective activity and intensifies precipitation within the rainband. The low-level inflow in this location is coupled with the locations of enhanced vorticity, rising motions, frontogenesis and evaporative cooling from previous stages.

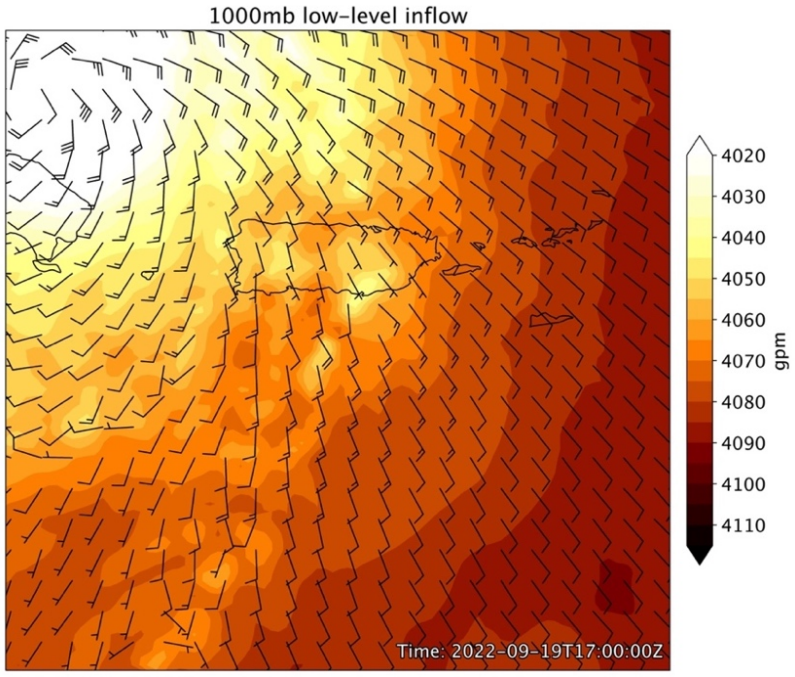

Figure 17. Low-level winds at 1000mb during S3 2022-09-19 at 2000 UTC.

Air and ocean temperature 2.3

Temperature gradients on pressure surfaces are analogous to pressure gradients on isentropic surfaces. Therefore, we examine the air temperature at 850 mb both before and after landfall at the same level to interpret our results from a different perspective. In Figure 18a, pre-landfall temperatures are approximately 2 K warmer than those in Figure 18b post-landfall, specifically south of the island. This area shows the most pronounced temperature difference, likely due to evaporative cooling following the heavy rainfall event. As discussed in our methodology, HAFSB is an ocean-hurricane coupled model, so changes in sea surface temperature (SST) are also noticeable. Figures 18c and 18d reveal a significant difference in SST between pre-landfall and post-landfall conditions; however, further investigation into the model is necessary to determine whether this cooling is caused by ocean mixing, strong upwelling, or storm-driven inertial waves.

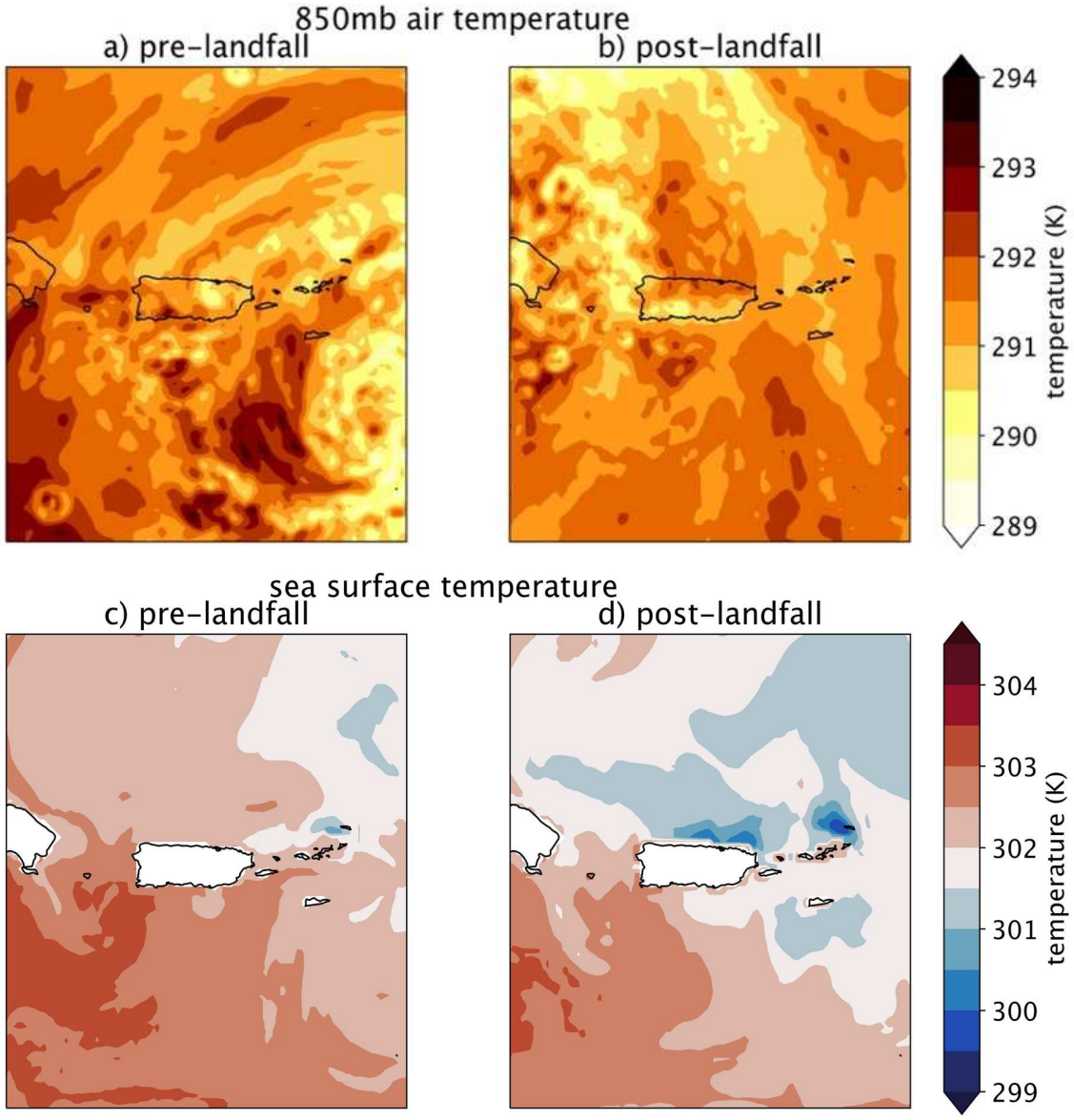

Figure 18. (a) Air temperature prior to landfall at 850mb. (b) Air temperature after landfall at 850mb. (c) Sea surface temperature prior to landfall. (b) Sea surface temperature post landfall.

SUMMARY DISCUSSION AND CONCLUSIONS

The asymmetrical precipitation structure of Hurricane Fiona, influenced by moderate VWS, reveals considerable variability in rainfall distribution across different phases of the storm: landfall effects, primary rainband activity, and the development of the tail-rainband. The analysis was divided in three stages to attribute dominant precipitation mechanisms from landfall to post-landfall. Precipitation accumulation discrepancies between ground observations and the HAFSB model simulations are primarily attributed to track differences. During the initial stage (S1), intense rainfall in the inner core, driven by strong convective updrafts, was concentrated over southern and eastern parts of the island in the HAFSB simulation. Airborne TDR observations confirm that the simulated structure closely resembled the real storm's structure; however, the simulation exhibited slightly more intense rainfall over northern and eastern Puerto Rico, as well as adjacent ocean regions. In S1, vigorous updrafts were observed within the asymmetric eyewall and outer rainbands, indicating strong convective activity associated with enhanced positive absolute vorticity in the eyewall itself and the storm-scale overturning circulation.

As Fiona interacted with land during S2, the intensity of vertical motions diminished slightly, reflecting the disruptive influence of land on the storm's structure. This phase was dominated by stratiform precipitation from the outer core and primary rainband, contributing significantly to rainfall over northern, eastern, and western Puerto Rico. Moderate VWS and land interaction aided to displace vorticity to the east resulting in vorticity advection that helped develop the principal rainband. S2 helped establish a more favorable environment for the redevelopment of the rainband in stage S3. This stage is distinguished by a broad area of upward motion that emerged south of Puerto Rico, where the tail rainband was most active. Despite the storm's interaction with land, convective processes remained strong, sustaining the redevelopment of

rainbands. Concentrated rainfall in southern Puerto Rico was influenced by both isentropic lifting and orographic effects, especially over the central mountains. These different lifting mechanisms and thermodynamic processes in each of the three stages modified Fiona's structure and led to diverse rainfall patterns across the island.

A schematic summarizing the main lifting mechanisms enhancing tail-rainband convection is presented in Figure 19. S1 and S2 set up a favorable environment for these mechanisms to produce heavy rainfall over waters, and over the island. Wind blowing from the southwest strengthens the detached tail-rainband over the ocean prior to reaching the southern coast of the island by isentropic lifting, then lifting is reinforced by the CMR and the orography of the island. On the leeward side of the mountain, enhancement ceases slightly, but afterwards convection is regenerated over waters by the modulated environment in S1 and S2 leading to isentropic lifting.

The evolution of Fiona's tail rainband is analyzed in detail, utilizing temperature gradients, absolute vorticity analyses, energy terms, vertical motion patterns, and frontogenesis calculations, all highlighting the intricate interplay of dynamic and thermodynamic factors. Isentropic lifting and evaporative cooling due to prior rainfall were critical in shaping the storm's tail-rainband, enhancing vertical motions both south and north of Puerto Rico. Additional mechanisms included low-level inflow, frontogenesis, and associated vorticity, which was displaced at upper levels by VWS. Orographic lifting from the island's topography also contributed to rainband development. Thermodynamic analyses at higher atmospheric levels revealed a link between convective heating and upward motion, underscoring the role of atmospheric stability and energy transport in maintaining the storm's intensity. These findings offer a comprehensive view of the factors influencing Fiona's tail-rainband evolution, emphasizing the interactions between atmospheric

dynamics, thermodynamics, and the effects of vertical wind shear on precipitation and vorticity structure.

A novel contribution of this research is its detailed description and understanding of the mechanisms driving Hurricane Fiona's destructive rainfall and how positive feedbacks from those different mechanisms enhanced the rainfall. The strong vorticity associated with the eyewall led to boundary layer inflow and the classical overturning circulation and heavy rainfall traditionally associated with a tropical cyclone. The mid-level vorticity generated in the eyewall was displaced by VWS, which promoted long-lasting asymmetric rainband rainfall after the storm center moved to the west of Puerto Rico. That rainfall then led to the pre-conditioning the environment for the subsequent development of a sloping isentropic surface through substantial evaporative cooling. The interaction with the broader southerly cyclonic flow with that sloping isentrope led to adiabatic ascent which brought air parcels to saturation and allowed them to release their convective instability. This finding in particular is novel since larger-scale meridional temperature gradients are not typically associated with tropical cyclones in the Caribbean. The presence of the complex terrain of the island itself enhanced the rainfall on the windward side and decreased the rainfall on the leeward side throughout all three stages of the event. The analysis presented here highlights the complexity of interactions that can lead to an extreme rainfall event and can help forecasters identify crucial mechanisms in future events.

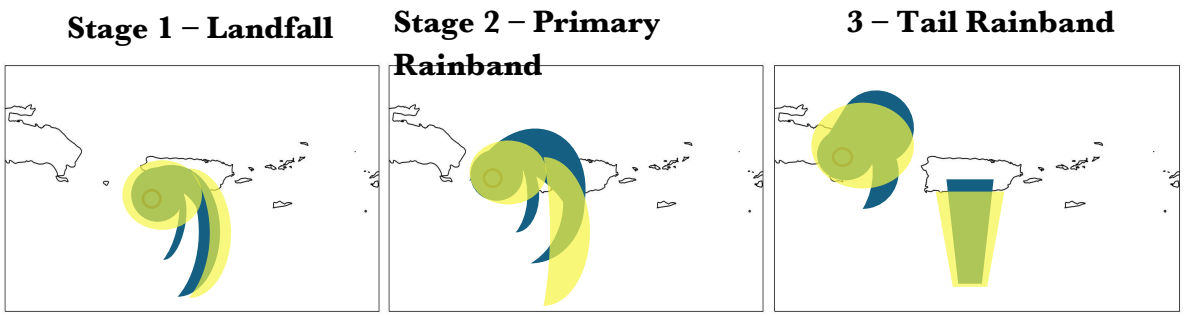

Figure 19. Schematic of the lifting mechanisms over Puerto Rico per stage. Yellow shading indicates absolute vorticity and blue shading indicates convection.

REFERENCES

Alaka, G. J., X. Zhang, and S. G. Gopalakrishnan, 2022: High-Definition Hurricanes: Improving Forecasts with Storm-Following Nests. *Bulletin of the American Meteorological Society*, **103**, E680–E703, https://doi.org/10.1175/BAMS-D-20-0134.1.

Alvey III, G. R., and A. Hazelton, 2022: How Do Weak, Misaligned Tropical Cyclones Evolve Toward Alignment? A Multi-Case Study Using the Hurricane Analysis and Forecast System. *Journal of Geophysical Research: Atmospheres*, **127**, e2022JD037268, https://doi.org/10.1029/2022JD037268.

Arias, I., and V. Chandrasekar, 2018: Cross Validation of GPM and Ground-Based Radar in Latin America and the Caribbean. *IGARSS 2018 - 2018 IEEE International Geoscience and Remote Sensing Symposium*, IGARSS 2018 - 2018 IEEE International Geoscience and Remote Sensing Symposium, 3891–3893.

Bernardet, L., and Coauthors, Hurricane Weather Research and Forecasting (HWRF) Model: 2014 Scientific Documentation.

Bleck, R., 2002: An oceanic general circulation model framed in hybrid isopycnic-Cartesian coordinates. *Ocean Modelling*, **4**, 55–88, https://doi.org/10.1016/S1463-5003(01)00012-9.

Boehm, A. M., and M. M. Bell, 2021: Retrieved Thermodynamic Structure of Hurricane Rita (2005) from Airborne Multi–Doppler Radar Data. *Journal of the Atmospheric Sciences*, **78**, 1583–1605, https://doi.org/10.1175/JAS-D-20-0195.1.

Cha, T.-Y., and M. M. Bell, 2021: Comparison of single-Doppler and multiple-Doppler wind retrievals in Hurricane Matthew (2016). *Atmospheric Measurement Techniques*, **14**, 3523–3539, https://doi.org/10.5194/amt-14-3523-2021.

——, ——, and A. J. DesRosiers, 2021: Doppler Radar Analysis of the Eyewall Replacement Cycle of Hurricane Matthew (2016) in Vertical Wind Shear. *Monthly Weather Review*, **149**, 2927–2943, https://doi.org/10.1175/MWR-D-20-0289.1.

Cheng, J., and Q. Li, 2020: A numerical study of convective-scale downdrafts in the outer core of tropical cyclones in vertically varying environmental flows. *Tropical Cyclone Research and Review*, **9**, 143–161, https://doi.org/10.1016/j.tcrr.2020.06.002.

Cheung, K., and Coauthors, 2018: Recent Advances in Research and Forecasting of Tropical Cyclone Rainfall. *Tropical Cyclone Research and Review*, **7**, 106–127, https://doi.org/10.6057/2018TCRR02.03.

Davies, H. C., 2015: The Quasigeostrophic Omega Equation: Reappraisal, Refinements, and Relevance. *Monthly Weather Review*, **143**, 3–25, https://doi.org/10.1175/MWR-D-14-00098.1.

DesRosiers, A. J., M. M. Bell, and T.-Y. Cha, 2022: Vertical Vortex Development in Hurricane Michael (2018) during Rapid Intensification. *Monthly Weather Review*, **150**, 99–114, https://doi.org/10.1175/MWR-D-21-0098.1.

Doswell, C. A., H. E. Brooks, and R. A. Maddox, 1996a: Flash Flood Forecasting: An Ingredients-Based Methodology. *Weather and Forecasting*, **11**, 560–581, https://doi.org/10.1175/1520-0434(1996)011<0560:FFFAIB>2.0.CO;2.

——, ——, and ——, 1996b: Flash Flood Forecasting: An Ingredients-Based Methodology. *Weather and Forecasting*, **11**, 560–581, https://doi.org/10.1175/1520-0434(1996)011<0560:FFFAIB>2.0.CO;2.

Dougherty, E., and K. L. Rasmussen, 2019: Climatology of Flood-Producing Storms and Their Associated Rainfall Characteristics in the United States. *Monthly Weather Review*, **147**, 3861–3877, https://doi.org/10.1175/MWR-D-19-0020.1.

Franklin, C. N., G. J. Holland, and P. T. May, 2005: Sensitivity of Tropical Cyclone Rainbands to Ice-Phase Microphysics. *Monthly Weather Review*, **133**, 2473–2493, https://doi.org/10.1175/MWR2989.1.

——, ——, and ——, 2006: Mechanisms for the Generation of Mesoscale Vorticity Features in Tropical Cyclone Rainbands. *Monthly Weather Review*, **134**, 2649–2669, https://doi.org/10.1175/MWR3222.1.

Gray, W. M., 1982: Tropical Cyclone Genesis and Intensification. *Intense Atmospheric Vortices*, L. Bengtsson and J. Lighthill, Eds., Berlin, Heidelberg, Springer, 3–20.

Gray, W. M., 2012: Fundamental Importance of Convective Downdrafts and Mass Recycling Within the Tropical Cloud Cluster and the Typhoon-Hurricane. *Tropical Cyclone Research and Review*, **1**, 130–141, https://doi.org/10.6057/2012TCRR01.14.

Hazelton, A., and Coauthors, 2022: Performance of 2020 Real-Time Atlantic Hurricane Forecasts from High-Resolution Global-Nested Hurricane Models: HAFS-globalnest and GFDL T-SHiELD. *Weather and Forecasting*, **37**, 143–161, https://doi.org/10.1175/WAF-D-21-0102.1.

——, and Coauthors, 2023: 2022 real-time Hurricane forecasts from an experimental version of the Hurricane analysis and forecast system (HAFSV0.3S). *Front. Earth Sci.*, **11**, https://doi.org/10.3389/feart.2023.1264969.

Hosannah, N., P. Ramamurthy, J. Marti, J. Munoz, and J. E. González, 2021: Impacts of Hurricane Maria on Land and Convection Modification Over Puerto Rico. *Journal of Geophysical Research: Atmospheres*, **126**, e2020JD032493, https://doi.org/10.1029/2020JD032493.

Houze, R. A., 1997: Stratiform Precipitation in Regions of Convection: A Meteorological Paradox? *Bulletin of the American Meteorological Society*, **78**, 2179–2196, https://doi.org/10.1175/1520-0477(1997)078<2179:SPIROC>2.0.CO;2.

——, and Coauthors, 2006: The Hurricane Rainband and Intensity Change Experiment: Observations and Modeling of Hurricanes Katrina, Ophelia, and Rita. *Bulletin of the American Meteorological Society*, **87**, 1503–1522, https://doi.org/10.1175/BAMS-87-11-1503.

Keellings, D., and J. J. Hernández Ayala, 2019: Extreme Rainfall Associated With Hurricane Maria Over Puerto Rico and Its Connections to Climate Variability and Change. *Geophysical Research Letters*, **46**, 2964–2973, https://doi.org/10.1029/2019GL082077.

Klotzbach, P. J., K. M. Wood, C. J. Schreck, S. G. Bowen, C. M. Patricola, and M. M. Bell, 2022: Trends in Global Tropical Cyclone Activity: 1990–2021. Geophysical Research Letters, **49**, e2021GL095774, https://doi.org/10.1029/2021GL095774.

Knaff, J. A., C. R. Sampson, P. J. Fitzpatrick, Y. Jin, and C. M. Hill, 2011: Simple Diagnosis of Tropical Cyclone Structure via Pressure Gradients. Weather and Forecasting, **26**, 1020–1031, https://doi.org/10.1175/WAF-D-11-00013.1.

Lai, H.-W., C. A. Davis, and B. J.-D. Jou, 2011: A Subtropical Oceanic Mesoscale Convective Vortex Observed during SoWMEX/TiMREX. Monthly Weather Review, **139**, 2367–2385, https://doi.org/10.1175/2010MWR3411.1.

Li, Q., Y. Wang, and Y. Duan, 2015: Impacts of Evaporation of Rainwater on Tropical Cyclone Structure and Intensity—A Revisit. Journal of the Atmospheric Sciences, **72**, 1323–1345, https://doi.org/10.1175/JAS-D-14-0224.1.

Liang, J., L. Wu, X. Ge, and C.-C. Wu, 2011: Monsoonal Influence on Typhoon Morakot (2009). Part II: Numerical Study. Journal of the Atmospheric Sciences, **68**, 2222–2235, https://doi.org/10.1175/2011JAS3731.1.

May, P. T., and G. J. Holland, 1999: The Role of Potential Vorticity Generation in Tropical Cyclone Rainbands. Journal of the Atmospheric Sciences, **56**, 1224–1228, https://doi.org/10.1175/1520-0469(1999)056<1224:TROPVG>2.0.CO;2.

Mazurek, A. C., and R. S. Schumacher, 2023: Quantifying the Relationship between Embedded Rotation and Extreme Rainfall Rates in Observations of Tropical Storm Imelda (2019). Monthly Weather Review, **151**, 1109–1128, https://doi.org/10.1175/MWR-D-22-0115.1.

Morin, M. J., and M. D. Parker, 2011: A numerical investigation of supercells in landfalling tropical cyclones. Geophysical Research Letters, **38**, https://doi.org/10.1029/2011GL047448.

Nguyen, L. T., J. Molinari, and D. Thomas, 2014: Evaluation of Tropical Cyclone Center Identification Methods in Numerical Models. Monthly Weather Review, **142**, 4326–4339, https://doi.org/10.1175/MWR-D-14-00044.1.

Nugent, A. D., and R. Rios-Berrios, 2018: Factors Leading to Extreme Precipitation on Dominica from Tropical Storm Erika (2015). Monthly Weather Review, **146**, 525–541, https://doi.org/10.1175/MWR-D-17-0242.1.

Ramos Scharrón, C. E., J. J. Hernández Ayala, E. Y. Arima, and F. Russell, 2023: Preliminary Analyses of the Hydro-Meteorological Characteristics of Hurricane Fiona in Puerto Rico. Hydrology, **10**, 40, https://doi.org/10.3390/hydrology10020040.

Rappaport, E. N., 2014: Fatalities in the United States from Atlantic Tropical Cyclones: New Data and Interpretation. *Bulletin of the American Meteorological Society*, **95**, 341–346, https://doi.org/10.1175/BAMS-D-12-00074.1.

Scatena, F. N., and M. C. Larsen, 1991: Physical Aspects of Hurricane Hugo in Puerto Rico. *Biotropica*, **23**, 317, https://doi.org/10.2307/2388247.

Schultz, D. M., 2010: How to Research and Write Effective Case Studies in Meteorology. *E-Journal of Severe Storms Meteorology*, **5**, 1–18, https://doi.org/10.55599/ejssm.v5i2.22.

Schumacher, R. S., 2017: Heavy Rainfall and Flash Flooding. *Oxford Research Encyclopedia of Natural Hazard Science*, Oxford University Press.

——, and R. H. Johnson, 2005: Organization and Environmental Properties of Extreme-Rain-Producing Mesoscale Convective Systems. *Monthly Weather Review*, **133**, 961–976, https://doi.org/10.1175/MWR2899.1.

Smith, A. B., 2020: U.S. Billion-dollar Weather and Climate Disasters, 1980 - present (NCEI Accession 0209268). https://doi.org/10.25921/STKW-7W73.

Smith, J. A., M. L. Baeck, Y. Su, M. Liu, and G. A. Vecchi, 2023: Strange Storms: Rainfall Extremes From the Remnants of Hurricane Ida (2021) in the Northeastern US. *Water Resources Research*, **59**, e2022WR033934, https://doi.org/10.1029/2022WR033934.

Takagi, H., and W. Wu, 2016: Maximum wind radius estimated by the 50 kt radius: improvement of storm surge forecasting over the western North Pacific. *Natural Hazards and Earth System Sciences*, **16**, 705–717, https://doi.org/10.5194/nhess-16-705-2016.

Tang, X., W.-C. Lee, and M. Bell, 2014: A Squall-Line-Like Principal Rainband in Typhoon Hagupit (2008) Observed by Airborne Doppler Radar. *Journal of the Atmospheric Sciences*, **71**, 2733–2746, https://doi.org/10.1175/JAS-D-13-0307.1.

Touma, D., S. Stevenson, S. J. Camargo, D. E. Horton, and N. S. Diffenbaugh, 2019: Variations in the Intensity and Spatial Extent of Tropical Cyclone Precipitation. *Geophysical Research Letters*, **46**, 13992–14002, https://doi.org/10.1029/2019GL083452.

Wang, C.-C., H.-C. Kuo, R. H. Johnson, C.-Y. Lee, S.-Y. Huang, and Y.-H. Chen, 2015: A numerical study of convection in rainbands of Typhoon Morakot (2009) with extreme rainfall: roles of pressure perturbations with low-level wind maxima. *Atmospheric Chemistry and Physics*, **15**, 11097–11115, https://doi.org/10.5194/acp-15-11097-2015.

Wu, L., J. Liang, and C.-C. Wu, 2011: Monsoonal Influence on Typhoon Morakot (2009). Part I: Observational Analysis. *Journal of the Atmospheric Sciences*, **68**, 2208–2221, https://doi.org/10.1175/2011JAS3730.1.

Xi, D., S. Wang, and N. Lin, 2022: Analyzing Relationships between Tropical Cyclone Intensity and Rain Rate over the Ocean Using Numerical Simulations. *Journal of Climate*, **36**, 81–91, https://doi.org/10.1175/JCLI-D-22-0141.1.

Xu, W., E. J. Zipser, Y.-L. Chen, C. Liu, Y.-C. Liou, W.-C. Lee, and B. J.-D. Jou, 2012: An Orography-Associated Extreme Rainfall Event during TiMREX: Initiation, Storm Evolution, and Maintenance. *Monthly Weather Review*, **140**, 2555–2574, https://doi.org/10.1175/MWR-D-11-00208.1.

Yu, C.-L., B. Tang, and R. G. Fovell, 2023: Tropical Cyclone Tilt and Precession in Moderate Shear: Precession Hiatus in a Critical Shear Regime. *Journal of the Atmospheric Sciences*, **80**, 909–932, https://doi.org/10.1175/JAS-D-22-0200.1.